Simulation of Alfvén eigenmode bursts using a hybrid code for nonlinear magnetohydrodynamics and energetic particles

Y. Todo[1,2], H.L. Berk[3] and B.N. Breizman[3]

[1] National Institute for Fusion Science, Toki, Japan
[2] Department of Fusion Science, The Graduate University for Advanced Studies
(SOKENDAI), Toki, Japan
[3] Institute for Fusion Studies, University of Texas at Austin, Austin, TX, USA

E-mail: todo@nifs.ac.jp

Abstract

A hybrid simulation code for nonlinear magnetohydrodynamics (MHD) and energetic-particle dynamics has been extended to simulate recurrent bursts of Alfvén eigenmodes by implementing the energetic-particle source, collisions and losses. The Alfvén eigenmode bursts with synchronization of multiple modes and beam ion losses at each burst are successfully simulated with nonlinear MHD effects for the physics condition similar to a reduced simulation for a TFTR experiment (Wong *et al* 1991 *Phys. Rev. Lett.* **66** 1874, Todo *et al* 2003 *Phys. Plasmas* **10** 2888). It is demonstrated with a comparison between nonlinear MHD and linear MHD simulation results that the nonlinear MHD effects significantly reduce both the saturation amplitude of the Alfvén eigenmodes and the beam ion losses. Two types of time evolution are found depending on the MHD dissipation coefficients, namely viscosity, resistivity and diffusivity. The Alfvén eigenmode bursts take place for higher dissipation coefficients with roughly 10% drop in stored beam energy and the maximum amplitude of the dominant magnetic fluctuation harmonic $\delta B_{m/n}/B \sim 5 \times 10^{-3}$ at the mode peak location inside the plasma. Quadratic dependence of beam ion loss rate on magnetic fluctuation amplitude is found for the bursting evolution in the nonlinear MHD simulation. For lower dissipation coefficients, the amplitude of the Alfvén eigenmodes is at steady levels $\delta B_{m/n}/B \sim 2 \times 10^{-3}$ and the beam ion losses take place continuously. The beam ion pressure profiles are similar among the different dissipation coefficients, and the stored beam energy is higher for higher dissipation coefficients.

1. Introduction

Energetic-particle transport and losses enhanced by Alfvén eigenmodes are an important concern for burning plasmas. Computer simulation is a powerful tool to investigate the interaction between Alfvén eigenmodes and energetic particles. We performed the first numerical demonstration of toroidal Alfvén eigenmode (TAE) bursts with parameters similar to a TFTR experiment and reproduced many of the experimental characteristics [1, 2]. These include (a) the synchronization of multiple TAEs, (b) modulation depth of the drop in the stored beam energy and (c) the stored beam energy. It was demonstrated by the surface of section plots that both the resonance overlap of different eigenmodes [3] and the disappearance of Kolmogorov–Arnold–Moser (KAM) surfaces in phase space due to overlap of higher order islands

created by a single eigenmode lead to particle loss. However, the saturation amplitude $\delta B/B \sim 2 \times 10^{-2}$ in the simulation results is higher than the value $\delta B/B \sim 10^{-3}$ which we inferred [2] from the plasma displacement that was measured in the plasma edge region with normalized radius $\rho > 0.8$ [4]. In the experiment, the plasma displacement (ξ) was estimated from the density fluctuation (δn) measurement assuming a relation $\xi \sim \delta n/(\partial n/\partial r)$ where $\partial n/\partial r$ is the radial gradient of the equilibrium density profile. In the region close to the plasma centre, $|\partial n/\partial r|$ is very small and the error bars for the displacement become infinitely large [4]. A possibility where the TAE saturation amplitude in the central region is larger than $\delta B/B \sim 10^{-3}$, which is the amplitude in the edge region, is not excluded.

Recently, we investigated the nonlinear MHD effects on a single Alfvén eigenmode instability using hybrid simulations

of an MHD fluid interacting with energetic particles [5]. To clarify the role of the MHD nonlinearity, the nonlinear MHD results were compared with results from a linear MHD simulation, where only linear MHD equations were solved together with a nonlinear response of the energetic particles. When the TAE saturation level is $\delta B/B \leqslant 10^{-3}$, no significant difference was found between the results of the linear MHD and the nonlinear MHD simulations. On the other hand, when the TAE saturation level is $\delta B/B \sim 10^{-2}$ in the linear MHD simulation, the saturation level in the nonlinear MHD case is found to be reduced to half the result of the linear MHD simulation. We found that the nonlinearly generated $n = 0$ and the higher n modes provide increased energy dissipation that appears crucial for achieving a reduced TAE saturation level. The total dissipation of all the toroidal mode numbers increases before the saturation of the instability. The increased dissipation leads to a reduction in the saturation amplitude even though the damping rate of the $n = 4$ component, which was the original TAE carrier, slightly decreases before saturation. We emphasize that this is a new picture for the mechanism by which nonlinear MHD effects cause saturation that is different from the other works [6, 7].

There is still a need to investigate the nonlinear MHD effects in TAE bursts using realistic parameters. The challenge of this work is to demonstrate saturation amplitudes that are closer to the value inferred from the experimental plasma displacement measurements than the previous reduced simulation [2]. Computer simulations of multiple Alfvén eigenmodes taking account of nonlinear MHD effects have been conducted [7–10]. In one of the simulations [9], it was demonstrated that synchronized bursts of multiple TAEs take place with the saturation level of the dominant magnetic fluctuation harmonic $\delta B_{m/n}/B \sim 4 \times 10^{-3}$, although the parameters are not very close to the experiment. In the simulation results of the TAE bursts presented in [2], the energetic-particle loss takes place when the TAE amplitude reaches $\delta B/B \sim 5 \times 10^{-3}$ while the saturation amplitude is $\delta B/B \sim 2 \times 10^{-2}$. These previous studies encouraged us to simulate TAE bursts taking account of the nonlinear MHD effects using physics parameters similar to the TFTR experiment [1].

In this work, we have extended the MEGA code [11–13], which is a hybrid simulation code for an MHD fluid interacting with energetic particles, by implementing the energetic-particle source, collisions and losses. We study the nonlinear MHD effects on TAE bursts using two versions of the MEGA code. With the standard version of the MEGA code, the full nonlinear dynamics of both the MHD fluid and the energetic particles is simulated. In the other version of the MEGA code, only linear MHD equations are used while the nonlinear particle dynamics is retained. We refer to this version as the linear MHD simulation. It is demonstrated for physical parameters close to the TFTR experiment that the nonlinear MHD effects reduce the saturation amplitude to a level $\delta B_{m/n}/B \sim 5 \times 10^{-3}$ for the dominant harmonic of the radial magnetic fluctuation. The TAE bursts take place with a time interval close to the experiment. The stored beam energy drop associated with each burst has a modulation depth of roughly 10%, which is also close to the inferred experimental value of 7%.

2. Simulation model

Several hybrid simulation models have been constructed [14–18] to study the evolution of Alfvén eigenmodes destabilized by energetic particles. In the MEGA code, the bulk plasma is described by the nonlinear MHD equations and the energetic ions are simulated with the δf particle method. The MHD equations with the energetic-ion effects are given by

$$\frac{\partial \rho}{\partial t} = -\nabla \cdot (\rho \boldsymbol{v}) + \nu_n \Delta(\rho - \rho_{\mathrm{eq}}), \tag{1}$$

$$\rho \frac{\partial}{\partial t} \boldsymbol{v} = -\rho \vec{\omega} \times \boldsymbol{v} - \rho \nabla \left(\frac{v^2}{2}\right) - \nabla p + (\boldsymbol{j} - \boldsymbol{j}'_h) \times \boldsymbol{B}$$
$$+ \frac{4}{3} \nabla(\nu \rho \nabla \cdot \boldsymbol{v}) - \nabla \times (\nu \rho \vec{\omega}), \tag{2}$$

$$\frac{\partial \boldsymbol{B}}{\partial t} = -\nabla \times \boldsymbol{E}, \tag{3}$$

$$\frac{\partial p}{\partial t} = -\nabla \cdot (p\boldsymbol{v}) - (\gamma - 1)p\nabla \cdot \boldsymbol{v} + (\gamma - 1)$$
$$\times \left[\nu \rho \omega^2 + \frac{4}{3} \nu \rho (\nabla \cdot \boldsymbol{v})^2 + \eta \boldsymbol{j} \cdot (\boldsymbol{j} - \boldsymbol{j}_{\mathrm{eq}}) \right]$$
$$+ \nu_n \Delta(p - p_{\mathrm{eq}}), \tag{4}$$

$$\boldsymbol{E} = -\boldsymbol{v} \times \boldsymbol{B} + \eta(\boldsymbol{j} - \boldsymbol{j}_{\mathrm{eq}}), \tag{5}$$

$$\boldsymbol{j} = \frac{1}{\mu_0} \nabla \times \boldsymbol{B}, \tag{6}$$

$$\vec{\omega} = \nabla \times \boldsymbol{v}, \tag{7}$$

where μ_0 is the vacuum magnetic permeability, γ is the adiabatic constant, ν and ν_n are the artificial viscosity and diffusion coefficients chosen to maintain numerical stability and all the other quantities are conventional. The subscript 'eq' represents the equilibrium variables. The energetic ion contribution is included in the MHD momentum equation (equation (2)) as the energetic ion current density $\boldsymbol{j}'_h$. The energetic ion current density $\boldsymbol{j}'_h$ in equation (2) includes the contributions from parallel velocity, magnetic curvature and gradient drifts, and magnetization current. The $\boldsymbol{E} \times \boldsymbol{B}$ drift disappears in $\boldsymbol{j}'_h$ due to quasi-neutrality [11]. We see that the electromagnetic field is given by the standard MHD description. This model is accurate under the condition that the energetic-ion density is much less than the bulk plasma density. The MHD equations are solved using a fourth-order (in both space and time) finite difference scheme.

For the purposes of clarifying the nonlinear MHD effects, linear MHD calculations were performed. In the linear MHD equations, we use variables with δ such as δB that represent the fluctuations, for example $\delta B = B - B_{\mathrm{eq}}$. Fluid velocity $\boldsymbol{v}$ is also a fluctuation because there is no flow in the equilibrium. In the linear MHD equations, first-order terms of fluctuations are retained while the second and the higher order terms are neglected. Equation (1) is linearized neglecting a term with $\delta \rho \boldsymbol{v}$ to

$$\frac{\partial \rho}{\partial t} = -\nabla \cdot (\rho_{\mathrm{eq}} \boldsymbol{v}) + \nu_n \Delta \delta \rho. \tag{8}$$

The linear version of equation (2) is obtained neglecting the terms with $\delta\rho v$, $\vec{\omega} \times v$, v^2, $\delta j \times \delta B$, and so on:

$$\rho_{\text{eq}} \frac{\partial}{\partial t} v = -\nabla p + (j_{\text{eq}} - j'_{h\,\text{eq}}) \times \delta B + (\delta j - \delta j'_h) \times B_{\text{eq}}$$
$$+ \frac{4}{3} \nabla(\nu \rho_{\text{eq}} \nabla \cdot v) - \nabla \times (\nu \rho_{\text{eq}} \vec{\omega}). \tag{9}$$

Equations (3), (6) and (7) are the same for the linear MHD simulation. The linear equations transformed from equations (4) and (5) are

$$\frac{\partial p}{\partial t} = -\nabla \cdot (p_{\text{eq}} v) - (\gamma - 1) p_{\text{eq}} \nabla \cdot v + (\gamma - 1) \eta \delta j \cdot j_{\text{eq}}$$
$$+ \nu_n \Delta \delta p, \tag{10}$$

$$E = -v \times B_{\text{eq}} + \eta \delta j. \tag{11}$$

Here, we have neglected the terms with $\delta p v$, ω^2, $(\nabla \cdot v)^2$, δj^2 and $v \times \delta B$.

The energetic particles are simulated using the δf particle-in-cell method with time-dependent equilibrium distribution function f_0. Energetic-particle source, collisions and losses are implemented in the MEGA code. The drift-kinetic description [19] is employed for the energetic particles. The equations of guiding-centre motion for computational particle is identical to that for the physical particle given by

$$\frac{\mathrm{d}}{\mathrm{d}t} x = \{x, H\}, \tag{12}$$

$$\frac{\mathrm{d}}{\mathrm{d}t} v = \{v, H\} - \nu_s v \left(1 + \frac{v_c^3}{v^3}\right), \tag{13}$$

$$\frac{\mathrm{d}}{\mathrm{d}t} \lambda = \{\lambda, H\} + C, \tag{14}$$

where $\{ \}$ and H are the Poisson bracket and Hamiltonian H. Here, x, v, $\lambda (\equiv v_\parallel / v)$ are spatial coordinates, total velocity and pitch-angle variable. The explicit expression of the Hamiltonian dynamics part can be found in [12, 13]. The slowing-down rate ν_s is the inverse of the slowing-down time $\nu_s = 1/\tau_s$, and the critical velocity v_c is related to the critical energy by $E_c = \frac{1}{2} m_h v_c^2$ where m_h is the energetic-particle mass. The slowing-down time and the critical energy are given by [20]

$$\tau_s = 2.0 \times 10^{19} \frac{A_h T_e (\text{keV})^{3/2}}{Z_h^2 n_e (\text{m}^{-3}) \ln \Lambda_e} \text{(s)}, \tag{15}$$

$$E_c = 14.8 A_h T_e \left[\frac{\sum_i n_i (Z_i^2 / A_i) \ln \Lambda_i}{n_e \ln \Lambda_e} \right]^{2/3}, \tag{16}$$

where A and Z are the atomic and charge numbers, T and n are the temperature and number density, and $\ln \Lambda$ is the Coulomb logarithm with subscripts i,e, h for ion, electron and energetic particles, respectively. The summation in equation (16) is over all the bulk ion species. The pitch-angle scattering term C is introduced in equation (14). The pitch-angle scattering is implemented at the end of each time step of simulation using a Monte Carlo procedure [21], where a particle's pitch angle is altered according to the relation

$$\lambda_{\text{new}} = \lambda_{\text{old}}(1 - 2\nu_d \Delta t) \pm [(1 - \lambda_{\text{old}}^2) 2\nu_d \Delta t]^{1/2}, \tag{17}$$

where ν_d and Δt are the pitch-angle scattering rate and time step width, and $\pm$ denotes a randomly chosen sign with equal probability for plus and minus.

The evolution of the distribution function f with slowing down, pitch-angle scattering and a particle source S is described by

$$\frac{\partial}{\partial t} f + \{f, H\} - \nu_s \frac{\partial}{v^2 \partial v}[(v^3 + v_c^3)f]$$
$$- \nu_d \frac{\partial}{\partial \lambda} \left[(1 - \lambda^2) \frac{\partial}{\partial \lambda} f \right] = S(x, v, \lambda). \tag{18}$$

We divide the Hamiltonian H into H_0 the Hamiltonian in the equilibrium field and H_1 the perturbation. We describe an equilibrium distribution function f_0 which satisfies

$$\frac{\partial}{\partial t} f_0 + \{f_0, H_0\} - \nu_s \frac{\partial}{v^2 \partial v}[(v^3 + v_c^3)f_0]$$
$$- \nu_d \frac{\partial}{\partial \lambda} \left[(1 - \lambda^2) \frac{\partial}{\partial \lambda} f_0 \right] = S(x, v, \lambda). \tag{19}$$

Subtraction of equation (19) from equation (18) gives the evolution of the perturbative distribution function $\delta f = f - f_0$ by

$$\frac{\partial}{\partial t} \delta f + \{\delta f, H_0 + H_1\} + \{f_0, H_1\} - \nu_s \frac{\partial}{v^2 \partial v}[(v^3 + v_c^3)\delta f]$$
$$- \nu_d \frac{\partial}{\partial \lambda} \left[(1 - \lambda^2) \frac{\partial}{\partial \lambda} \delta f \right] = 0. \tag{20}$$

The evolution of δf along the computational particle orbit defined by equations (12)–(14) is expressed by

$$\frac{\mathrm{d}}{\mathrm{d}t} \delta f + \{f_0, H_1\} - 3\nu_s \delta f = 0. \tag{21}$$

Equations (12)–(14) do not satisfy Liouville's theorem because the slowing-down term is 'compressible' in phase space. Then, the phase space volume (V) occupied by each computational particle varies in time. We should consider the time evolution of V. The number of physical particles that each computational particle represents is given by fV. As the number of physical particles conserves along each computational particle orbit with an exception of the particle source, the evolution of fV follows

$$\frac{\mathrm{d}}{\mathrm{d}t}(fV) = SV. \tag{22}$$

Equations (22) and (18) rewritten to $(\mathrm{d}/\mathrm{d}t)f - 3\nu_s f = S$ give the evolution equation of V,

$$\frac{\mathrm{d}}{\mathrm{d}t} V = -3\nu_s V. \tag{23}$$

We solve the evolution of both δf and V for each computational particle.

A time-dependent solution of equation (19) should be specified in advance of the simulation. Firstly, let us find a solution that does not depend on the pitch-angle variable λ. Such a solution can be found for an energetic-particle source isotropic in velocity space with a spatial profile $h(r)$, which is a function of radial coordinate r,

$$S(r, v) = \frac{2\nu_s h(r)}{\sqrt{\pi} v^2 \Delta v} \exp\left[-\left(\frac{v - v_b}{\Delta v} \right)^2 \right], \tag{24}$$

where v_b is the beam injection velocity or the energetic-particle birth velocity, and the parameter Δv is chosen to be $0.05 v_b$ for numerical stability of the simulation of Alfvén eigenmodes. The Gaussian factor in equation (24) is reduced to a delta function $\delta(v - v_b)$ in a limit $\Delta v \to 0$. We can find the following time-dependent equilibrium solution neglecting the $\{f_0, H_0\}$ term:

$$f_0(\boldsymbol{x}, v, t) = \frac{h(r)}{(v^3 + v_c^3)} \left[\mathrm{erf}\left(\frac{v' - v_b}{\Delta v}\right) - \mathrm{erf}\left(\frac{v - v_b}{\Delta v}\right) \right],$$
(25)

$$v' = \{(v^3 + v_c^3) \exp[3\nu_s(t + t_{\mathrm{inj}})] - v_c^3\}^{1/3},$$
(26)

where $t = -t_{\mathrm{inj}} < 0$ is the time when the beam injection has started while the simulation starts at $t = 0$. The solution f_0 is a reasonable approximation for fusion alpha particles that are born isotropic in velocity space. The time-dependent distribution function given by equation (25) is reduced to the slowing-down distribution in a limit $t \to \infty$ and $\Delta v \to 0$,

$$f_0(\boldsymbol{x}, v, t) = \frac{2h(r)}{(v^3 + v_c^3)} \qquad (v \leqslant v_b)$$

$$= 0 \quad (v > v_b)$$
(27)

Secondly, let us find a solution that depends on the pitch angle. If we neglect the pitch-angle scattering and the finite orbit effects for f_0, we can find such a solution. We introduce another pitch-angle variable $\Lambda \equiv 2\mu B_0/mv^2 = (1 - \lambda^2) B_0/B$ where μ is the magnetic moment, B_0 and B are the magnetic field strength at the plasma centre and the particle location, respectively. If the energetic-particle source is given by

$$S(r, v, \Lambda) = \frac{2\nu_s h(r)}{\sqrt{\pi} v^2 \Delta v} \exp\left[-\left(\frac{v - v_b}{\Delta v}\right)^2 \right] g(\Lambda),$$
(28)

the time-dependent equilibrium distribution function is

$$f_0(\boldsymbol{x}, v, \Lambda, t) = \frac{h(r)}{(v^3 + v_c^3)} \left[\mathrm{erf}\left(\frac{v' - v_b}{\Delta v}\right) \right.$$

$$\left. - \mathrm{erf}\left(\frac{v - v_b}{\Delta v}\right) \right] g(\Lambda)$$
(29)

because $(\partial/\partial t)\Lambda = 0$, $\{\Lambda, H_0\} = 0$ and $(\partial/\partial v)\Lambda = 0$ hold in equation (19).

For fusion alpha particles, the time-dependent equilibrium given by equation (25) is a reasonable solution where the pitch-angle scattering is considered but the finite orbit width effects are neglected. When we neglect the pitch-angle scattering, the time-dependent equilibrium given by equation (29) is applicable to energetic ions created by neutral beam injection. The 1/2 and 1/3 energy components can be modelled if we adjust the value of v_b. The time-dependent equilibrium is expressed by the sum of the three injection energy components. The time-dependent equilibrium distribution for the ion cyclotron range of frequency (ICRF) heating is beyond the scope of this work because the ICRF significantly modifies the particle pitch angle resulting in highly anisotropic particle distributions in velocity space. For a more realistic equilibrium solution that takes account of the finite orbit width effects and pitch-angle scattering, we should resort to the numerical analysis of f_0. In this work, we present the results using the

analytical equilibrium solution f_0 given by equation (29) with $g(\Lambda) = \delta(\Lambda) = \delta(|\lambda| - 1)$.

In the δf particle simulation, the computational particles should cover the whole phase space. Attention should be paid to the particle loss process. If the computational particles that reach the plasma boundary are just removed, the total phase space volume decreases by the volume covered by the lost particles. Then, alternative particles should be injected into the plasma to cover the lost phase space volume elements. However, it is not straightforward to find the injection location proper to the lost particles. One clear method is to follow all the lost particle orbits outside the plasma and return them into the plasma. Then, the whole phase space inside the plasma is covered by the computational particles of which orbits are closed. In this work we set the particle loss boundary at $r/a = 0.8$ inside the plasma and model particle loss by setting $\delta f = 0$ for the computational particles outside the loss boundary. The computational particles return across the loss boundary along the physical particle orbits, and the computation of δf is restarted with $\delta f = 0$ on the loss boundary. Phase space inside the plasma is now a part of a larger phase space that is covered by the computational particles of closed orbits. If the simulation domain is extended to include the vacuum region, the loss boundary can be set at a more realistic location.

The coordinates employed in the simulation are cylindrical coordinates (R, φ, z). The shape of the outermost magnetic surface is circular. The bulk plasma density is uniform. The number of grid points for the cylindrical coordinates (R, φ, z) is $128 \times 64 \times 128$ and the number of computational particles is $N = 6.6 \times 10^5$. For the purposes of data analysis, magnetic flux coordinates (r, φ, ϑ), where ϑ is the poloidal angle, were constructed for the MHD equilibrium. The equations of motion and the evolution of δf and V for each computational particle are solved using a fourth-order Runge–Kutta method. We do not employ Richardson's extrapolation although it improves the numerical accuracy if two calculations with different time steps are used. If we use calculations with time steps Δt and $\Delta t/2$, the total computational cost is tripled from a calculation with a single time step Δt. The computational particles are initially loaded randomly and uniformly in each (R, φ, z) direction so that the simulation domain is covered by the particles. The phase space volume and the major radius of ith particle $V_{\mathrm{loading}\,i}$ and $R_{\mathrm{loading}\,i}$ at the particle loading stage are related to each other by $V_{\mathrm{loading}\,i} = \alpha R_{\mathrm{loading}\,i}$ using a normalization factor α.

We perform the simulation of TAE bursts with parameters similar to a TFTR experiment [1]. The parameters are $a = 0.75$ m, $R_0 = 2.4$ m, $B_0 = 1$ T, beam injection energy is 110 keV, and NBI power (P_h) is 10 MW. Both the bulk and beam ions are deuterium. The bulk ion density is 2.8×10^{19} m^{-3}. The beam injection velocity corresponds to $v_b = 1.1 v_A$. The safety factor profile and beam injection profile are assumed as the same as in [2], $q(r) = 1.2 + 1.8(r/a)^2$ and $h(r) = \exp[-(r/0.4a)^2]$, respectively. The slowing-down time and the critical velocity are assumed to be 100 ms and $v_c = 0.65 v_A$, respectively. The beam velocity is purely parallel to the magnetic field to model the parallel beam injection. The pitch-angle scattering is neglected. At all the time of the simulation, the equilibrium distribution function f_0 given

by equation (27) should be fully covered by the computational particles. Then, at the injection time $t = -t_{\text{inj}}$, the velocity space $v_{\min 0} \equiv v_{\text{b}} - 3\Delta v \leqslant v \leqslant v_{\text{b}} + 3\Delta v \equiv v_{\max 0}$ is filled with the computational particles. The computational particles are injected with a velocity $v = v_{\max 0}$. We can define the time $t = -t_{\text{start}}$ when the particle with $v = v_{\min 0}$ at $t = -t_{\text{inj}}$ is injected at $v = v_{\max 0}$. The time t_{start} is given by

$$t_{\text{start}} = \ln[(v_{\max 0}^3 + v_{\text{c}}^3)/(v_{\min 0}^3 + v_{\text{c}}^3)]/3\nu_{\text{s}} + t_{\text{inj}}. \qquad (30)$$

The computational particles are injected with a constant time interval. The injection time of the ith marker particle ($1 \leqslant i \leqslant N$) is given by

$$t_i = (t_{\text{start}} + t_{\text{end}})i/N - t_{\text{start}}, \qquad (31)$$

where t_{end} is the ending time of the simulation. For the computational particles with $t_i \leqslant 0$, the initial velocity at $t = 0$ is $v_i(t = 0) = v_{\text{c}}\{[(v_{\max 0}/v_{\text{c}})^3 + 1]\exp(3\nu_{\text{s}}t_i) - 1\}^{1/3}$. For the ith computational particle with $t_i > 0$, the particle is injected at $t = t_i$ with $v(t = t_i) = v_{\max 0}$. After $t = t_i$, the calculation for the ith computational particle is performed. The energetic-particle parallel pressure at a grid point located at $\boldsymbol{x} = \boldsymbol{x}_k$, which enters into the energetic-particle current density $\boldsymbol{j}'_h$ through the curvature drift, is calculated by

$$p_{h\|}(\boldsymbol{x}_k, t) = \sum_{i=1}^N m_h v_{\|i}^2 [f_0(\boldsymbol{x}_i, \boldsymbol{v}_i, t) + \delta f(\boldsymbol{x}_i, \boldsymbol{v}_i, t)]$$
$$\times V_i(t)A(\boldsymbol{x}_k - \boldsymbol{x}_i)\Theta(t - t_i)/(R_k \Delta R \Delta\varphi \Delta z), \qquad (32)$$

where $A(\boldsymbol{x}_k - \boldsymbol{x}_i)$ is the shape factor of the particle-in-cell method and $\Theta(t - t_i)$ is the Heaviside function, and $\Delta R, \Delta\varphi, \Delta z$ are grid spans of each direction. For the energetic-particle current density $\boldsymbol{j}'_h$, we use only the fluctuation part of the energetic-particle pressure

$$\delta p_{h\|}(\boldsymbol{x}_k, t) = \sum_{i=1}^N m_h v_{\|i}^2 \delta f(\boldsymbol{x}_i, \boldsymbol{v}_i, t)V_i(t)A(\boldsymbol{x}_k - \boldsymbol{x}_i)$$
$$\times \Theta(t - t_i)/(R_k \Delta R \Delta\varphi \Delta z), \qquad (33)$$

because the temporal increase in energetic-particle pressure due to the evolution of f_0 modifies the plasma equilibrium. The normalization factor α, which gives $V_{\text{loading } i}$ by $V_{\text{loading } i} = \alpha R_{\text{loading } i}$, is determined to be consistent with the heating power neglecting the terms of the order of $O(\varepsilon^2)$ with $\varepsilon = \Delta v/v_{\text{b}}$ by

$$P_h = \sum_{i=1}^N V_{\text{loading } i}\frac{1}{2}m_h v_{\text{b}}^2 \frac{h(r_{\text{loading } i})}{(v_{\text{b}}^3 + v_{\text{c}}^3)(t_{\text{start}} + t_{\text{end}})}, \qquad (34)$$

where $r_{\text{loading } i}$ is the radial coordinate at the particle loading stage. The initial phase space volume is given by $V_i(t = 0) = V_{\text{loading } i}[v_i(t = 0)^3 + v_{\text{c}}^3]/(v_{\text{b}}^3 + v_{\text{c}}^3)$ for the ith particle with $t_i \leqslant 0$ and $V_i(t = t_i) = V_{\text{loading } i}(v_{\max 0}^3 + v_{\text{c}}^3)/(v_{\text{b}}^3 + v_{\text{c}}^3)$ for $t_i > 0$, to be consistent with the slowing-down process. The spatial locations are the same as those at the particle loading stage and $\delta f = 0$ at $t = 0$ for the particles with $t_i \leqslant 0$ and at $t = t_i$ for the particles with $t_i > 0$. If we load the computational particles completely uniformly in configuration space with $V_{\text{loading } i} = $ const. and approximate $V_i(t)$ by $V_i(t) = V_{\text{loading } i}[v_i(t)^3 + v_{\text{c}}^3]/(v_{\text{b}}^3 + v_{\text{c}}^3)$, this simulation scheme approaches that developed in [22]. However, the evolution
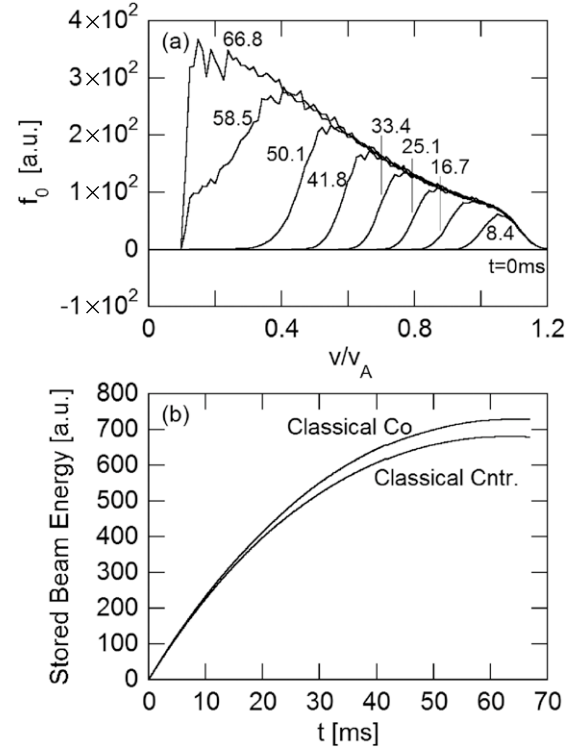

Figure 1. Time evolution of (*a*) beam ion distribution function and (*b*) stored beam energy for the co- and counter-injected beams in a classical simulation.

of $v_i(t)$ which is given by equation (13) is affected by the Hamiltonian (collisionless) dynamics whereas the evolution of $V_i(t)$ is caused only by the slowing-down collisions as is given in equation (23). Then, it is not clear whether the phase space volume of each computational particle $V_i(t)$ can be simply related to $v_i(t)$. This is the reason why we compute the evolution of $V_i(t)$ using equation (23). The computation of $V_i(t)$, the time-dependent f_0 and the modelling of particle losses are the new features of the present scheme compared with the scheme developed in [22].

A classical simulation where there is no MHD fluctuation was performed using the physics condition mentioned above and $t_{\text{inj}} = 0$ ms. The particle orbits are followed in the equilibrium magnetic field taking account of the slowing-down collisions. The computational particles are removed when they slow down to $v_i(t) = 0.1v_{\text{A}}$. The time evolutions of the beam ion distribution function and of the stored beam energy for co- and counter-injected beams are shown in figure 1. The distribution function in the figure is calculated on grid points $v = v_k$ evenly spaced in velocity by

$$f_{0\text{sim}}(v_k, t) = \sum_{i=1}^N f_0(\boldsymbol{x}_i, \boldsymbol{v}_i, t)V_i(t)A_v(v_k - v_i)\Theta(t - t_i)/v_k^2, \qquad (35)$$

where $A_v(v_k - v_i)$ assigns each particle to the nearest velocity grid point. We see the formation process of the slowing-down distribution in figure 1(*a*). In figure 1(*b*), the stored beam energy is saturated around $t = 60$ ms at levels roughly 700 in the unit of the figure for each of the co- and counter-beams.
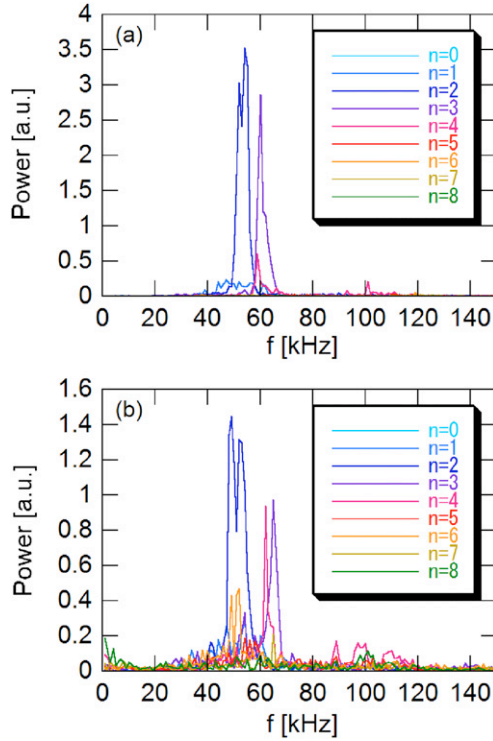
Figure 2. Frequency spectra of radial velocity harmonics with $m/n = 0/0$, 2/1, 3/2, 5/3, 7/4, 8/5, 10/6, 12/7 and 13/8 at $r/a = 0.5$ from $t = 0$ to 10 ms for (*a*) linear MHD and (*b*) nonlinear MHD simulations.
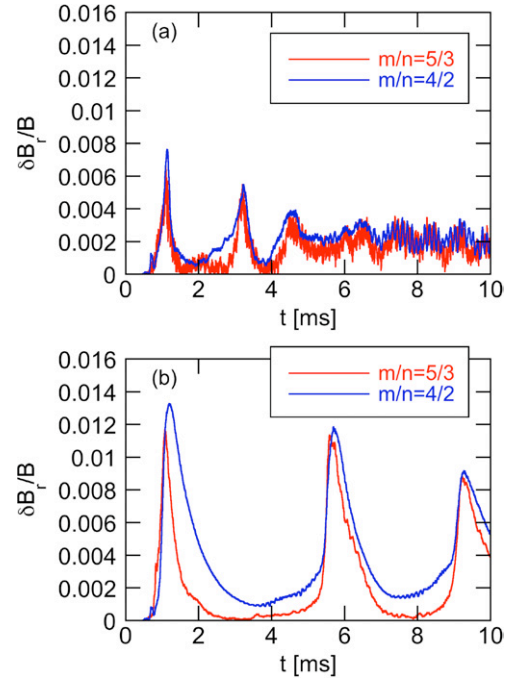
3. Simulation results

3.1. Comparison of nonlinear and linear MHD runs

We compare the results of a nonlinear MHD run and a linear MHD run for the dissipation coefficients $\nu = \nu_n = \eta/\mu_0 = 10^{-7} v_A R_0$. In this work, viscosity, diffusion and resistivity in the MHD equations are set to be equal to each other, $\nu = \nu_n = \eta/\mu_0$. Frequency spectra of radial velocity harmonics with $m/n = 0/0$, 2/1, 3/2, 5/3, 7/4, 8/5, 10/6, 12/7 and 13/8 at $r/a = 0.5$ from $t = 0$ to 10 ms are shown in figure 2 for (*a*) linear MHD and (*b*) nonlinear MHD simulations. The TAE modes with toroidal mode numbers $n = 2$ and 3 are dominant in the simulation results. In the nonlinear MHD simulation, the modes with toroidal mode numbers $n = 4$ and 6 also have substantial amplitude. It is interesting to note that there are peaks of $n = 4$ mode at higher frequency ~ 100 kHz. These can be produced by the nonlinear coupling of the dominant $n = 2$ mode. We see such a high-frequency peak also in the TFTR experiment result shown in figure 2 of [1]. The spatial profiles of the two dominant TAE modes at $t = 3.2$ ms in the nonlinear MHD run are shown in figure 3. The amplitude evolutions of the dominant radial magnetic fluctuation harmonics with $m/n = 4/2$ and $m/n = 5/3$ at each peak location inside the plasma are shown for the nonlinear MHD and the linear MHD runs in figure 4. We see in figure 4(*a*) that the synchronized TAE bursts take place three times at $t = 1.1$, 3.2 and 4.5 ms. The amplitude of the first burst is $\delta B_r/B \sim 8 \times 10^{-3}$ for $m/n = 4/2$ harmonic and $\delta B_r/B \sim 6 \times 10^{-3}$ for $m/n = 5/3$ harmonic. After the third burst, the amplitude of the two TAE modes reach steady
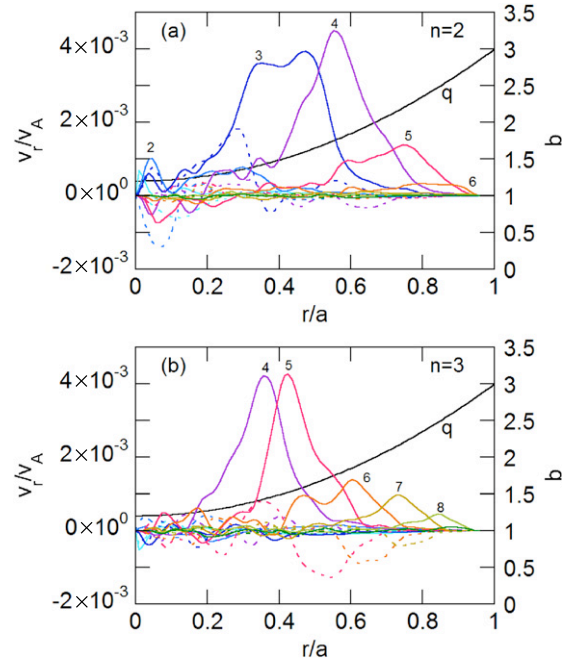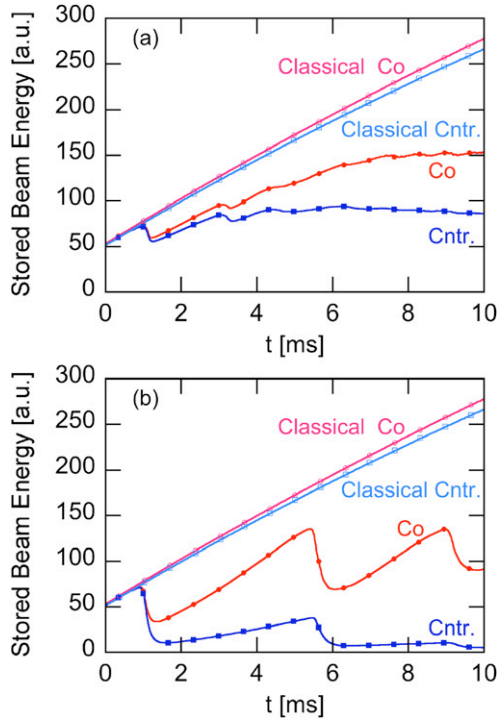

Figure 3. Radial velocity profiles of each poloidal harmonic of the TAEs with toroidal mode numbers for (*a*) $n = 2$ and (*b*) $n = 3$ at $t = 3.2$ ms in the nonlinear MHD run. Solid (dashed) lines show $\cos(m\vartheta + n\varphi)$ [$\sin(m\vartheta + n\varphi)$] harmonics with poloidal mode number m labelled in the figure.

Figure 4. Evolution of the dominant radial magnetic fluctuation harmonics with $m/n = 4/2$ and $m/n = 5/3$ at each peak location for (*a*) nonlinear MHD run and (*b*) linear MHD run with $\nu = \nu_n = \eta/\mu_0 = 10^{-7} v_A R_0$.

levels $\delta B_r/B \sim 2 \times 10^{-3}$. In the linear MHD simulation result shown in figure 4(*b*), three synchronized TAE bursts take place with an average time interval of 4 ms. The amplitude of the first burst is $\delta B_r/B \sim 1.3 \times 10^{-2}$ for $m/n = 4/2$ harmonic and $\delta B_r/B \sim 1.2 \times 10^{-2}$ for $m/n = 5/3$ harmonic.

Figure 6. Stored beam energy loss rate versus radial magnetic fluctuation amplitude with $m/n = 4/2$ at $0 \leqslant t \leqslant 3$ ms for nonlinear MHD and linear MHD runs. Arrows represent direction of time. Data points are plotted every 0.03 ms.

Figure 5. Stored energy evolution of co- and counter-beams with classical stored beam energy evolution for (*a*) nonlinear MHD run and (*b*) linear MHD run with $\nu = \nu_n = \eta/\mu_0 = 10^{-7} v_A R_0$.

The time evolutions of the stored beam energy for nonlinear MHD and linear MHD runs are shown in figure 5 together with the classical simulation where there is no MHD fluctuation. We see in figure 5(*a*) the drops in stored beam energy at the first burst by 18% for the co-injected beam and by 23% for the counter-injected beam. The stored beam energy reaches steady levels at $t = 10$ ms while the classical stored beam energy continues to increase. The saturation levels of stored energy for the co-injected and the counter-injected beams are, respectively, 22% and 12% of the classical saturation levels shown in figure 1. For the linear MHD run, we see in figure 5(*b*) the drops in the stored beam energy at the first burst by 53% for the co-injected beam and by 85% for the counter-injected beam. The drops in the linear MHD run are significantly larger than those in the nonlinear run. The results of the linear MHD and nonlinear MHD runs shown in figures 4 and 5 demonstrate that the amplitude of the TAE modes and the beam ion losses induced by the TAE modes are significantly reduced by the nonlinear MHD effects. The drop in the stored counter-beam energy is larger than that of the co-beam, and the stored counter-beam energy reaches lower levels in both the linear and nonlinear MHD runs. The asymmetry in the beam ion loss between the co- and counter-beams may arise from the fact that the counter-beam (co-beam) interacts primarily with the TAE poloidal harmonic $m + 1$ (m) when the major poloidal harmonics are m and $m + 1$. As the $m + 1$ harmonic is located radially on the outer side, the counter-beam ions are more likely to be lost by the TAE modes.

To see the nonlinear MHD effects more clearly, the stored beam energy loss rate is plotted versus radial magnetic fluctuation amplitude with $m/n = 4/2$ at $0 \leqslant t \leqslant 3$ ms for the nonlinear MHD and linear MHD runs in figure 6. The stored
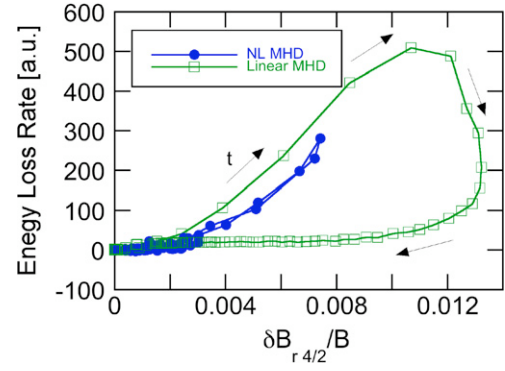
beam energy loss rate plotted in the figure is a component due to the particle losses and is roughly in proportion to the beam ion loss rate. We see the curve for the linear MHD run forms a large loop in the figure that corresponds to the large magnetic fluctuation amplitude and the large beam ion loss rate. On the other hand, the curve for the nonlinear MHD run extends along the curve for the linear MHD run, but is limited in the region of the small magnetic fluctuation amplitude and the small beam ion loss rate. It is interesting to note that the energy loss rate for the nonlinear MHD run traces the same trajectory both when the magnetic fluctuation grows and damps. There is a one-to-one relationship between the magnetic fluctuation amplitude and the beam ion loss rate for the nonlinear MHD run. However, the one-to-one relationship does not apply to the linear MHD result. The beam ion loss rate decreases while the magnetic fluctuation amplitude is maintained at $\delta B_r/B \geqslant 10^{-2}$. Significant beam ion redistribution and losses have already taken place, and lead to the saturation and decrease in the beam ion loss rate.

3.2. Dependence on dissipation

The nonlinear MHD run described in section 3.1 was continued from $t = 9.85$ ms with the same dissipation coefficients $\nu = \nu_n = \eta/\mu_0 = 10^{-7} v_A R_0$ and two different coefficients $3 \times 10^{-7} v_A R_0$ and $5 \times 10^{-7} v_A R_0$. The beam injection continues to the end of the simulation. The amplitude evolution of the dominant radial magnetic fluctuation harmonics with $m/n = 4/2$ and $m/n = 5/3$ is shown in figure 7. For $\nu = \nu_n = \eta/\mu_0 = 10^{-7} v_A R_0$ and $3 \times 10^{-7} v_A R_0$, the amplitude of the dominant radial magnetic fluctuation harmonics with $m/n = 4/2$ and $m/n = 5/3$ is at steady levels, $\delta B_r/B \sim 2 \times 10^{-3}$. One slight difference is that the magnetic fluctuation level with $m/n = 4/2$ shown in figure 7(*b*) is higher than that shown in figure 7(*a*). For $\nu = \nu_n = \eta/\mu_0 = 5 \times 10^{-7} v_A R_0$, the time evolution shown in figure 7(*c*) is qualitatively different from the lower dissipation coefficient cases. Five TAE bursts take place with an average time interval of 1.7 ms. The average maximum amplitude of the dominant radial magnetic fluctuation harmonics with $m/n = 4/2$ is $\delta B_r/B \sim 5 \times 10^{-3}$.
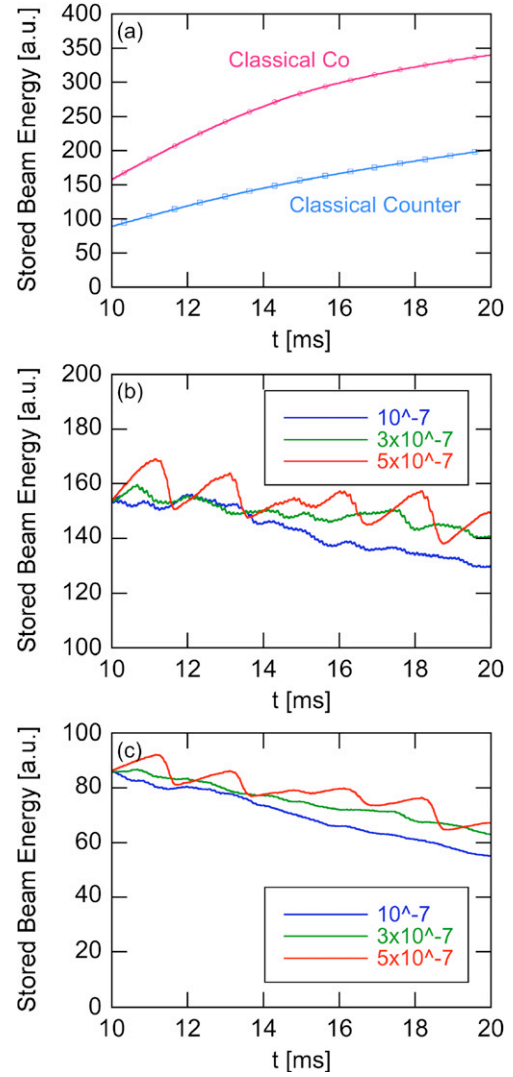
The stored beam energy evolution is compared among the different dissipation coefficients in figure 8. A classical simulation where there is no MHD fluctuation was also
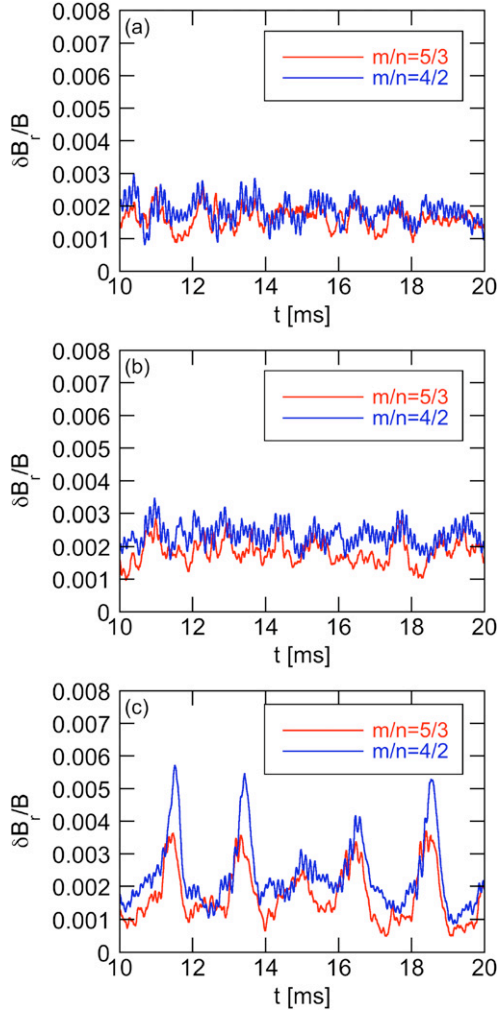
Figure 7. Evolution of the dominant radial magnetic fluctuation harmonics with $m/n = 4/2$ and $m/n = 5/3$ at each peak location for nonlinear MHD run with (*a*) $\nu = \nu_n = \eta/\mu_0 = 10^{-7}v_A R_0$, (*b*) $3 \times 10^{-7}v_A R_0$ and (*c*) $5 \times 10^{-7}v_A R_0$.

Figure 8. Stored energy evolution of (*a*) classical co- and counter-beams, and (*b*) co- and (*c*) counter-beams for nonlinear MHD runs with $\nu = \nu_n = \eta/\mu_0 = 10^{-7}v_A R_0$, $3 \times 10^{-7}v_A R_0$ and $5 \times 10^{-7}v_A R_0$.

performed starting from the same condition at $t = 9.85$ ms. Figure 8(*a*) shows that the classical stored beam energy increases in time due to the continuous beam injection. On the other hand, we see in figures 8(*b*) and (*c*) that the stored energy of co- and counter-beams gradually decreases for the lower dissipation coefficients. Then, we know that the gradual decrease in the stored beam energy is brought about by the MHD fluctuations. We can conclude that the TAE modes with the steady amplitude $\delta B_r/B \sim 2 \times 10^{-3}$ cause significant beam ion losses that balance with the continuous beam injection. For $\nu = \nu_n = \eta/\mu_0 = 5 \times 10^{-7}v_A R_0$, we see drops in the stored beam energy associated with the TAE bursts in figures 8(*b*) and (*c*). For the last TAE burst, the total stored beam energy drops by 13% from $t = 18.2$ to 18.8 ms.
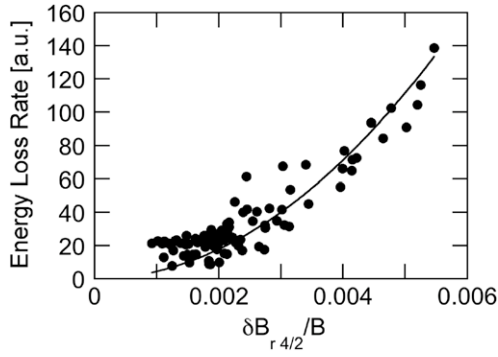
The stored beam energy loss rate is plotted versus radial magnetic fluctuation amplitude with $m/n = 4/2$ at $10 \leqslant t \leqslant$ 20 ms for $\nu = \nu_n = \eta/\mu_0 = 5 \times 10^{-7}v_A R_0$ in figure 9. The stored beam energy loss rate plotted in the figure is a component due to the particle losses and is roughly in proportion to the beam ion loss rate. We see in figure 9 that the beam ion loss rate can be fitted well with a quadratic function of the

magnetic fluctuation amplitude. The quadratic dependence is consistent with the beam ion losses due to the resonance overlap of the multiple TAE modes. We investigate as to how the beam ion beta profile depends on the dissipation. The beam beta profiles at $t = 20$ ms for the different dissipation coefficients are compared in figure 10. The shape of the profiles looks similar to each other. This suggests that the beam beta profiles are close to a marginal stability state. However, the absolute value is higher for higher dissipation coefficients. The higher dissipation coefficients reduce the TAE mode growth rate, and also lead to the bursting behaviour and to the higher stored beam energy. The results indicate that the stabilization of the TAE modes is essential to keep the stored beam energy higher even when the time evolution is bursting. More attention should be paid to the steady amplitude TAE modes for energetic-particle confinement. Even if the amplitude of the steady modes is low, it can result in significant beam ion losses through resonance overlap of the multiple modes, and can reduce the stored beam energy.

Figure 9. Stored beam energy loss rate versus radial magnetic fluctuation amplitude with $m/n = 4/2$ at $10 \leqslant t \leqslant 20$ ms for nonlinear MHD run with $\nu = \nu_n = \eta/\mu_0 = 5 \times 10^{-7} v_A R_0$. Data points are plotted every 0.1 ms. Solid line is a quadratic fit to the data.
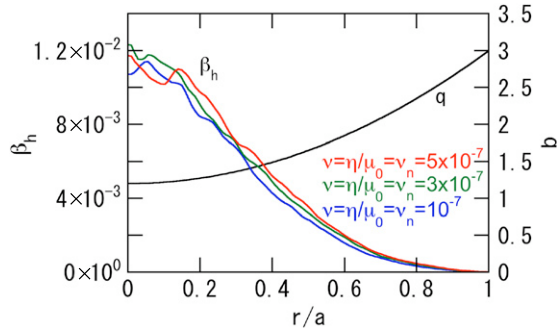
Figure 10. Comparison of beam ion beta profile for different dissipation coefficients at $t = 20$ ms.

4. Discussion and summary

The MEGA code, a hybrid simulation code for nonlinear magnetohydrodynamics (MHD) and energetic-particle dynamics, has been extended to simulate recurrent bursts of Alfvén eigenmodes by implementing the energetic-particle source, collisions and losses. The Alfvén eigenmode bursts with synchronization of multiple modes and beam ion losses at each burst have been successfully simulated with nonlinear MHD effects for the physics condition similar to a reduced simulation for a TFTR experiment. It was demonstrated with a comparison between the nonlinear MHD and linear MHD simulations that the nonlinear MHD effects significantly reduce both the saturation amplitude of the Alfvén eigenmodes and the beam ion losses. Two types of time evolution were found depending on the MHD dissipation coefficients, namely viscosity, resistivity and diffusivity. The Alfvén eigenmode bursts take place for higher dissipation coefficients with roughly 10% drop in the stored beam energy and the maximum amplitude of the dominant magnetic fluctuation harmonic $\delta B_{m/n}/B \sim 5 \times 10^{-3}$ at the mode peak location inside the plasma. When the dissipation coefficients are low, the amplitude of the Alfvén eigenmodes is at steady levels with $\delta B_{m/n}/B \sim 2 \times 10^{-3}$ inducing beam ion losses. In both types of evolutions, the stored beam energy is saturated at levels of 15% of that of the classical simulation without MHD fluctuations. The spatial profiles of the beam ion pressure are similar among the different dissipation coefficient cases, and the stored beam energy is lower for the

steady amplitude evolution than for the bursting evolution. For the bursting evolution in the nonlinear MHD simulation, we found the beam ion loss rate has a quadratic dependence on the magnetic fluctuation amplitude. The quadratic dependence is consistent with the particle losses due to the resonance overlap of the multiple Alfvén eigenmodes.

The saturation level of the stored beam energy in this work is lower than that in the previous reduced simulation, where the stored beam energy was about 40% of the classical level [2]. This difference may arise from the particle loss boundary set at $r/a = 0.8$ in the present simulations while it was modelled in the previous work by taking account of a limiter on which the plasma leans on the strong field side but which permits the co-injected beam ions to excurse outside the plasma. Such a realistic loss condition will lead to a higher saturation level of the stored beam energy. We also simplified the beam ion velocity distribution completely parallel to the magnetic field, and neglected the 1/2 and 1/3 energy components. The finite Larmor radius effects of the beam ions were also not considered. These simplifications enhance the energetic-particle drive to the Alfvén eigenmodes. If we improve these points, the time interval of the bursts will become longer because the energetic-particle drive is reduced. Let us point out a possibility that the threshold value in dissipation coefficients for the bursting evolution may be reduced for the weak energetic-particle drive with the improved beam distribution, and a bursting evolution may appear for the lower dissipation coefficients with the burst time interval close to that found in this paper. The analytic time-dependent solution of the energetic-particle equilibrium distribution function was obtained in this work. The solution can apply to fusion alpha particles with pitch-angle scattering taken into account, and also to beam ions if we neglect pitch-angle scattering. For more general energetic ions including ICRF-heated ions, numerical solutions are needed for the time-dependent equilibrium distribution.

Recently, an anomalous flattening of the beam ion spatial profile was observed in the central region of the DIII-D plasma with reversed magnetic shear [23]. The flattening of the beam ion spatial profile has been reproduced by a computer simulation where multiple TAE modes and reversed shear Alfvén eigenmodes are used with amplitude fixed constant [24, 25]. The amplitude $\delta B/B \sim 2 \times 10^{-4}$ used in [24, 25] is consistent with the measurement in the DIII-D experiment. Large neutron deficits that indicate significant beam ion losses were also observed on DIII-D and ASDEX Upgrade [26]. In this paper, we obtained qualitatively similar results with the steady amplitude of multiple Alfvén eigenmodes accompanied by significant beam ion losses. We also found the quadratic dependence of the energetic-particle loss rate on the magnetic fluctuation amplitude for the bursting evolution. The quadratic dependence of energetic-particle loss rate on magnetic fluctuation amplitude was observed on ASDEX Upgrade for the incoherent losses due to multiple Alfvén eigenmodes and for the losses induced by a single Alfvén eigenmode with amplitude larger than a threshold [27]. The quadratic dependence is also observed for particle losses induced by a single Alfvén eigenmode on LHD [28]. The quadratic dependence indicates the emergence of stochasticity in phase space. Simulations with more detailed modelling

of the energetic-particle distribution are needed to reproduce the up-to-date experimental observations and clarify how stochasticity emerges for the lost particles observed on the fast ion loss detectors.

Acknowledgments

References

[1] Wong K.L. *et al* 1991 *Phys. Rev. Lett.* **66** 1874
[2] Todo Y., Berk H.L. and Breizman B.N. 2003 *Phys. Plasmas* **10** 2888
[3] Berk H.L., Breizman B.N. and Pekker M.S. 1995 *Nucl. Fusion* **35** 1713
[4] Durst R.D., Fonck R.J., Wong K.L., Cheng C.Z., Fredrickson E.D. and Paul S.F. 1992 *Phys. Fluids* B **4** 3707
[5] Todo Y., Berk H.L. and Breizman B.N. 2010 *Nucl. Fusion* **50** 084016
[6] Zonca F., Romanelli F., Vlad G. and Kar C. 1995 *Phys. Rev. Lett.* **74** 698
[7] Spong D.A., Carreras B.A. and Hedrick C.L. 1994 *Phys. Plasmas* **1** 1503
[8] Fu G.Y. and Park W. 1995 *Phys. Rev. Lett.* **74** 1594
[9] Todo Y., Watanabe T.-H., Park H.-B. and Sato T. 2001 *Nucl. Fusion* **41** 1153
[10] Vlad G. *et al* 2009 *Nucl. Fusion* **49** 075024
[11] Todo Y. and Sato T. 1998 *Phys. Plasmas* **5** 1321
[12] Todo Y., Shinohara K., Takechi M. and Ishikawa M. 2005 *Phys. Plasmas* **12** 012503
[13] Todo Y. 2006 *Phys. Plasmas* **13** 082503
[14] Park W. *et al* 1992 *Phys. Fluids* B **4** 2033
[15] Spong D.A., Carreras B.A. and Hedrick C.L. 1992 *Phys. Fluids* B **4** 3316
[16] Todo Y., Sato T., Watanabe K., Watanabe T.H. and Horiuchi R. 1995 *Phys. Plasmas* **2** 2711
[17] Briguglio S., Vlad G., Zonca F. and Kar C. 1995 *Phys. Plasmas* **2** 3711
[18] Wang X., Zonca F. and Chen L. 2010 *Plasma Phys. Control. Fusion* **52** 115005
[19] Littlejohn R.G. 1983 *J. Plasma Phys.* **29** 111
[20] Heidbrink W.W. and Sadler G.J. 1994 *Nucl. Fusion* **34** 535
[21] Boozer A.H. and Kuo-Petravic G. 1981 *Phys. Fluids* **24** 851
[22] Lang J., Fu G.Y. and Chen Y. 2010 *Phys. Plasmas* **17** 042309
[23] Heidbrink W.W. *et al* 2007 *Phys. Rev. Lett.* **99** 245002
[24] White R.B., Gorelenkov N., Heidbrink W.W. and Van Zeeland M.A. 2010 *Phys. Plasmas* **17** 056107
[25] White R.B., Gorelenkov N., Heidbrink W.W. and Van Zeeland M.A. 2010 *Plasma Phys. Control. Fusion* **52** 045012
[26] Van Zeeland M.A. *et al* 2011 *Phys. Plasmas* **18** 056114
[27] García-Munoz *et al* 2010 *Phys. Rev. Lett.* **104** 185002
[28] Ogawa K. *et al* 2010 *Nucl. Fusion* **50** 084005